Applied Mathematical Modelling 96 (2021) 177–188

Contents lists available at ScienceDirect

Applied Mathematical Modelling

journal homepage: www.elsevier.com/locate/apm

Experimental and numerical optimization modelling to reduce radiofrequency-induced risks of magnetic resonance examinations on leaded implants

Juan Córcoles[a,*], Aiping Yao[b], Niels Kuster[c,d]

[a] Department of Electronic and Communications Technology, Universidad Autónoma de Madrid, C/ Fco. Tomás y Valiente, 11, Escuela Politécnica Superior, Madrid 28049, Spain
[b] School of Information Science and Engineering, Lanzhou University, No. 222, Tianshui South Road, Lanzhou, China
[c] Foundation for Research on Information Technologies in Society (IT'IS), Zurich, Zeughausstrasse, 43, 8004, Switzerland
[d] Department of Information Technology and Electrical Engineering, Swiss Federal Institute of Technology (ETH), Zurich, Raemistrasse 101, 8092, Switzerland

ARTICLE INFO

Article history:
Received 19 May 2020
Revised 21 February 2021
Accepted 24 February 2021
Available online 9 March 2021

Keywords:
Electromagnetic fields
Electromagnetic medical applications
Radiofrequency
Radiofrequency-induced heating
Numerical optimization
Finite-difference time-domain method

ABSTRACT

Convex formulations can be used to reduce the local specific absorption rate enhancement by active medical implants of radiofrequency fields in magnetic resonance examinations while minimizing the loss of image quality. This paper demonstrates that such an optimization methodology, previously presented for strictly computational models, can be extended to a hybrid scheme using experimentally determined implant models and pre-computed fields, which can enable quasi real-time exposure optimization. The methodology determines the optimum radiofrequency field shimming condition by considering both the reduction of specific absorption rate enhancement at the tip of the implant lead, created by the interaction of the radiofrequency fields tangential to the implant trajectory with the characteristic response of the implant, and the preservation of magnetic field homogeneity, which correlates to image quality. The inputs to this workflow are those required for each implant by standard ISO 10974 evaluation, namely the validated piecewise transfer function of the implant, the clinical routing within the patient, and the pre-computed numerical estimation of patient exposure without the implant. Optimized incident field conditions were computed to meet a range of numerical targets for specific absorption rate reduction, stepping down percentagewise from the maximum field homogeneity to the minimum exposure enhancement, for a generic implant with a flexible wire in a standard benchtop radiofrequency coil and phantom. Measurements of the corresponding specific absorption rate enhancements validated the predictions from the optimization approach within the combined confidence interval.

© 2021 The Authors. Published by Elsevier Inc.
This is an open access article under the CC BY-NC-ND license
(http://creativecommons.org/licenses/by-nc-nd/4.0/)

* Corresponding author.
E-mail address: juan.corcoles@uam.es (J. Córcoles).

https://doi.org/10.1016/j.apm.2021.02.036
0307-904X/© 2021 The Authors. Published by Elsevier Inc. This is an open access article under the CC BY-NC-ND license
(http://creativecommons.org/licenses/by-nc-nd/4.0/)

1. Introduction

Radiofrequency (RF)-induced heating of implantable medical devices during magnetic resonance (MR) examinations is a long-known major safety concern [1], in particular for patients with active implants that include an elongated conductive wire, such as neurostimulators, deep-brain stimulators and pacemakers. The RF electric field generated by MR systems causes high specific absorption rate (SAR) values, which are concentrated at hotspots, such as electrodes of elongated implants, leading to temperature increase in the surrounding tissues [2]. Compatibility of long, conductive implants, such as active implanted medical devices (AIMD), with MR examinations is currently evaluated according to the methods of ISO/TS 10974 [3], where a 4-Tier approach is proposed to assess the risk of RF-induced implant heating. Higher tiers reduce the overestimation of SAR with increased fidelity, at the expense of computational time. Tier 4, full-wave simulation of the implant model inside an anatomical phantom in an RF coil, is not affordable for every clinical exposure condition and implant routing. Tier 3 separates the RF-body interaction, which produces the incident fields to the implant, from the response of the implant to an arbitrary RF field. The latter can be modelled by an implant transfer function [4–6] which is applicable for different exposure configurations. Reduction of RF-induced SAR at the electrodes of the implant in MRI can generally be accomplished in two ways: (i) by carrying out a specific design of the implant (assuming the MRI RF-field exposure given by a two-channel excitation in quadrature) [7–10] and (ii) by modifying the MRI RF-exposure conditions [11–14]. To improve magnetic field homogeneity in the field of interest, MR systems allow the RF field to be 'shimmed' by adjusting the relative feed of RF coil channels. RF-shimming can also be used to reduce patient SAR for the general (non-implanted) population [15–18] as well as for implanted patients [13].

This work extends previously published convex formulations [13,19] to incorporate measured data and to experimentally validate the methodology. This hybrid method is an important step towards applicability of the method for quasi real-time optimization by the MRI scanners. For that purpose, the measured implant transfer function, derived for each implant as part of ISO 10974 Tier 3 evaluation, is combined with a computational model of an implant-free experimental setup. As a next step, a numerical convex optimization is performed, to obtain the exposure configuration that provides the desired SAR reduction while maximizing magnetic field homogeneity. We have then validated this approach in a simplified experimental setup.

2. Hybrid numerical-experimental methodology

The overall workflow of the proposed methodology is shown in Fig. 1. For each MR scanner channel (I and Q), the tangential electric field (E-field) to the implant along a desired routing in a phantom is derived from validated implant-free simulations. Then, the experimentally measured transfer function of the implant hotspot's response, $S(z)$ (where z stands for the position along the AIMD), is combined with these simulated tangential E-fields to estimate the response for each case. The range of channel relative amplitudes and phases is then optimized following formulations presented in [13,19] to find the field exposure configurations corresponding to the required SAR reduction at the implant electrode. For the experimental validation, these numerically derived exposure conditions are reproduced in the experimental setup (Section 2.4), with the implant present, by matching the overall radiofrequency magnetic field $\vec{B}_1$. Predicted SAR reduction near the implant electrode is validated by measurement of the SAR enhancement at the device tip. The agreement is assessed against the combined confidence interval of predictions and measurements.

2.1. Measurement of the implant transfer function

The generic implant used in this work is shown in Fig. 2. It consists of a 550 mm helical wire with a plastic material as insulation coat. One end of the lead has a metallic tip (electrode), the other connects to a metallic can.

In this work, the piecewise transfer function $S(z)$ [3] is measured with the Piecewise eXcitation System (piX System, ZMT Zurich MedTech AG), shown in Fig. 2. The implant is mounted in a phantom filled with tissue-simulating liquid, with electrical conductivity $\sigma = 0.47$ S/m and relative dielectric permittivity $\epsilon_r = 78$, as shown in Fig. 2. With the piX system, a

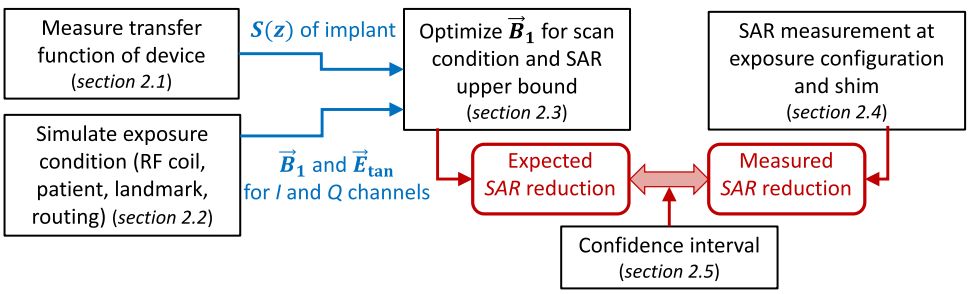

Fig. 1. Workflow of the validated hybrid numerical-experimental methodology for optimized RF-induced SAR mitigation.

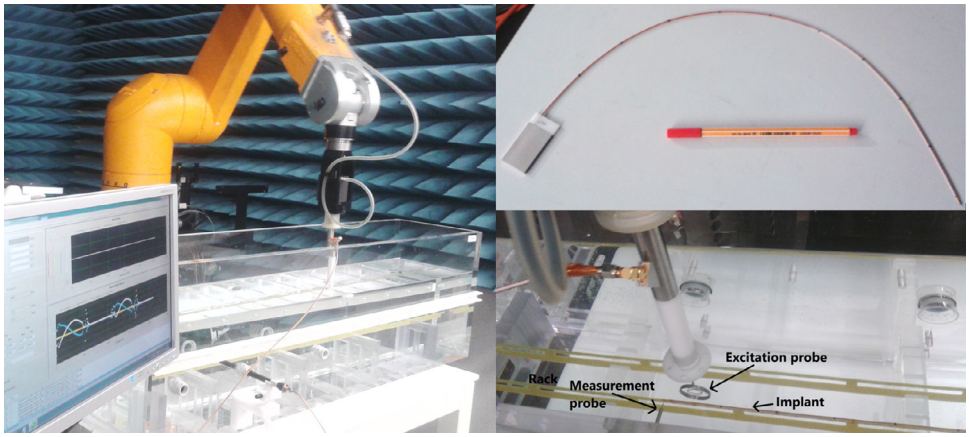

Fig. 2. Left: piX system for RF-heating evaluation of medical devices in MR examinations. Top Right: Generic 550 mm long implant (including the can) studied in this work. Bottom Right: Rack-mounted implant inside tissue-simulating liquid with excitation and measurements probes in the piX System to assess the transfer function $S(z)$.

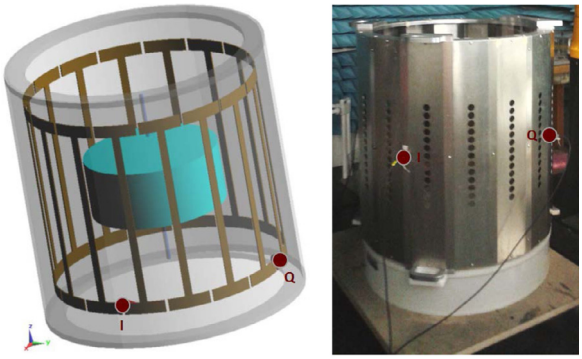

(a) (b)

Fig. 3. (a) Computational model of the RF coil and phantom, with red dots indicating feed locations. (b) MITS1.5T shielded 16-rung high-pass birdcage coil resonator operating close to 64 MHz.

localized tangential electric field pulse is applied every 10 mm with a moving excitation probe, while a field probe, located at the electrode of the implant, records the response of the tip electrode to the pulse applied at each position.

Once the piecewise transfer function $S(z)$ is measured, the power deposition at the hotspot of the AIMD P_{hotspot} can be estimated according to [3] as:

$$P_{\text{hotspot}} = A\left|\int_{z=0}^{l} S(z)E_{\tan}(z)\mathrm{d}z\right|^2, \tag{1}$$

where l is the length of the AIMD, A is a constant and $E_{\tan}$ is the tangential electric field to the implant under a specific exposure configuration.

2.2. Numerical simulation of implant-free experimental setup model

In order to experimentally demonstrate mitigation of the the RF-induced SAR through exposure definition, numerical models of the RF coil and phantoms are created. Fig. 3(a) shows the computational model used in this work which corresponds to the actual birdcage coil resonator, the MITS1.5 (ZMT), shown in Fig. 3(b), used for validation measurements in Section 2.4. The MITS1.5 resonator consists of a shielded 16-rung high-pass birdcage, with two channel feeds, I and Q (indicated by red coloured circles in Fig. 3). The birdcage is 65 cm long and has an inner diameter of 70 cm. A cylindrical phantom [6] filled with tissue simulating liquid ($\sigma = 0.47$ S/m and $\epsilon_r = 78$) is placed at the center of the birdcage. Numerical simulations are performed with the verified Finite-Difference Time-Domain (FDTD) solver in Sim4Life (ZMT), for which the model is discretized in approximately 34 million voxels (including absorbing boundary condition layers). The induced fields in the phantom generated at the resonant operating frequency (close to the ideal 63.8 MHz) by each of the two channels (I and Q) are computed. This FDTD simulation has to be run only once for a given birdcage, phantom, and scan position; implant trajectory and shimming are obtained by post-processing the FDTD results.

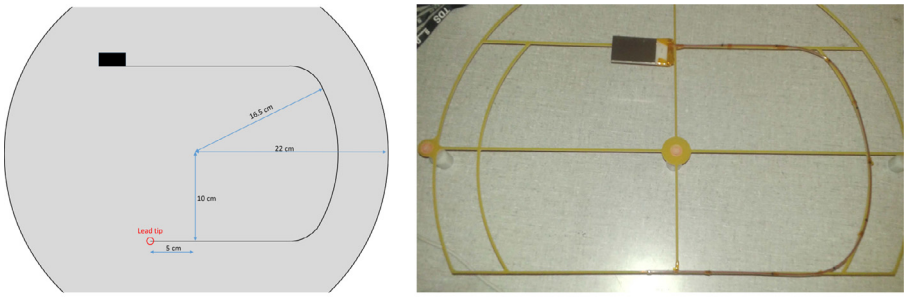

(a) (b)

Fig. 4. (a) Pathway used to extract the tangential electric field in the computational model in the cylindical phantom filled with tissue simulating medium (grey). (b) Mounted implant following a similar pathway for the experimental validation setup.

2.3. Field optimization of desired exposure configurations

Once the fields from the I and Q channels are computationally determined, the component of the $\vec{B}_1$ field rotating in the same direction as nuclear precession, defined as B_1^+ (right-hand circular polarization component of $\vec{B}_1$) at a location $\vec{r}_n$ and the tangential electric field to the implant routing at a position z_m along the trajectory can can be readily computed as weighted superpositions [13,19] from the 2×1 vector $\mathbf{v}$ of complex amplitudes of both channels $\mathbf{v} = [v_I, v_Q]^T$:

$$\vec{B}_1(\vec{r}_n) = \mathbf{b}_{\mathbf{1},n}^{+T}\mathbf{v}, \quad E_{\tan}(z_m) = \mathbf{e}_{\mathbf{tan},m}^T\mathbf{v} \tag{2}$$

where superscript T denotes the vector/matrix transpose, and $\mathbf{b}_{\mathbf{1},n}^+$ and $\mathbf{e}_{\mathbf{tan},m}$ are 2×1 vectors containing the B_1^+ and $E_{\tan}$ fields generated by each channel at the corresponding location $\vec{r}_n$ and position along the implant z_m:

$$\mathbf{b}_{\mathbf{1},n}^+ = \left[B_{1,I}^+(\vec{r}_n) \quad B_{1,Q}^+(\vec{r}_n)\right]^T, \ \mathbf{e}_{\mathbf{tan},m} = \left[E_{\tan,I}(z_m) \quad E_{\tan,Q}(z_m)\right]^T \tag{3}$$

The resulting power deposited at the tip hotspot can be calculated by incorporating the measured transfer function $S(z)$ and discretizing the integral in (1), by dividing the implant trajectory into M segments, as:

$$P_{\text{hotspot}} = A\left|\begin{bmatrix} S(z_1)\delta_1 \\ \vdots \\ S(z_m)\delta_m \\ \cdots \\ S(z_M)\delta_M \end{bmatrix}^T \begin{bmatrix} E_{\tan}(z_1) \\ \vdots \\ E_{\tan}(z_m) \\ \vdots \\ E_{\tan}(z_M) \end{bmatrix}\right|^2 = A\|\mathbf{S}_\delta^T\mathbf{E}_{\mathbf{tan}}\mathbf{v}\|^2 \tag{4}$$

where z_m is the centre position of each segment, while δ_m is the length of such a segment. $\mathbf{S}_\delta$ is the $M \times 1$ vector whose entries are $S(z_m)\delta_m$, as seen in (4), while $\mathbf{E}_{\mathbf{tan}}$ is the $M \times 2$ matrix defined as $\mathbf{E}_{\mathbf{tan}} = [\mathbf{e}_{\mathbf{tan},1}, \mathbf{e}_{\mathbf{tan},2}, \cdots, \mathbf{e}_{\mathbf{tan},M}]^T$. Symbol $\|\cdot\|$ denotes the L_2-norm. The SAR at a region around the hotspot can then be computed as $SAR = P_{\text{hotspot}}/\mathcal{M}$, where $\mathcal{M}$ is the mass of the considered region.

Taking the N voxels of the FDTD grid corresponding to the central slice of the the cylindrical phantom with tissue simulating liquid, the usual problem in MR to obtain set of excitations $\mathbf{v}_{\text{BH}}$ that achieve the best $|B_1^+|$ homogeneity in this central slice with respect to a reference (real positive) value $B_{1,\text{ref}}^+$ can be formulated as a matrix magnitude least-squares problem, which can be tackled with the local variable exchange method [20], where a succession of ordinary least-squares problems are solved [13] with the aid of an auxiliary vector $\mathbf{t}$:

$$\min_{\mathbf{v}} \quad \left\|\mathbf{B}_{\mathbf{1}}^+\mathbf{v} - B_{1,\text{ref}}^+\mathbf{t}\right\|^2 \Rightarrow \mathbf{v}_{\text{BH}} \tag{5}$$

where $\mathbf{B}_{\mathbf{1}}^+$ is the $N \times 2$ matrix defined as $\mathbf{B}_{\mathbf{1}}^+ = [\mathbf{b}_{\mathbf{1},1}^+, \mathbf{b}_{\mathbf{1},2}^+, \cdots \mathbf{b}_{\mathbf{1},N}^+]^T$, while the $N \times 1$ vector $\mathbf{t}$ has entries of the form $e^{j\phi_n}$, where the different phases ϕ_n take the value of the last iteration in the aforementioned local phase exchange method.

Starting from the best homogeneity situation given by $\mathbf{v}_{\text{BH}}$ (and the auxiliary vector $\mathbf{t}$ for further developments purposes), one of the formulations presented in [13] can be used to force a specified reduction (in percentage) in the induced power at the hotspot of the implant for a defined pathway inside the birdcage. The chosen pathway in this work, along which the tangential fields are extracted from the FDTD simulation, is shown in Fig. 4(a) [6]. This work considers three objective percentage reductions, i.e., 80%, 50% and 20%, whose formulation (constant A from (4) is dropped for ease of notation) and respective excitation vector solutions $\mathbf{v}_{80}, \mathbf{v}_{50}, \mathbf{v}_{20}$, are:

$$\begin{aligned} \min_{\mathbf{v}} \quad & \left\|\mathbf{B}_{\mathbf{1}}^+\mathbf{v} - B_{1,\text{ref}}^+\mathbf{t}\right\|^2 \\ \text{s.t.} \quad & \left\|\mathbf{S}_\delta^T\mathbf{E}_{\mathbf{tan}}\mathbf{v}\right\|^2 \le C\left\|\mathbf{S}_\delta^T\mathbf{E}_{\mathbf{tan}}\mathbf{v}_{\text{BH}}\right\|^2 \end{aligned} \Rightarrow \begin{cases} \mathbf{v}_{80}, \text{ for } C = 80\% \\ \mathbf{v}_{50}, \text{ for } C = 50\% \\ \mathbf{v}_{20}, \text{ for } C = 20\% \end{cases} \tag{6}$$

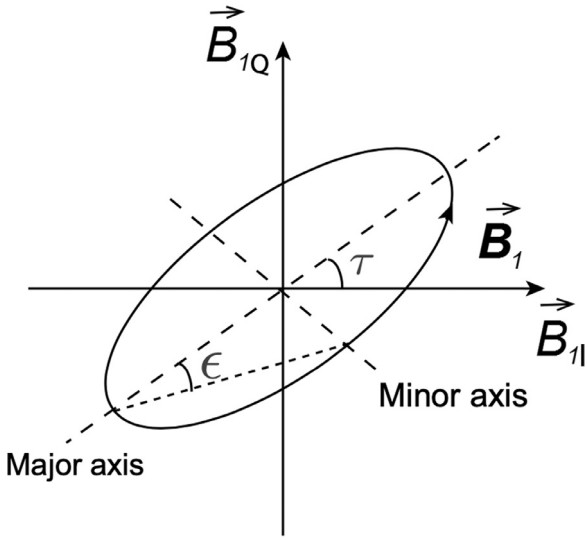

$$\epsilon = [-45°: 5°: 45°]$$

$$\tau = [0°: 10°: 180°]$$

Fig. 5. Illustration of the polarization ellipse of the RF magnetic field (ϵ and τ are two parameters used to characterize the ellipticity and tilt angle of the ellipse), and the parameter range of the explored polarizations.

Fig. 6. Experimental measurement setup including the implant inside the birdcage coil resonator as well as one time-domain magnetic field probe and one SAR probe from two different perspectives. [6].

where C is the *a-priori* set constant to aim at a specific SAR reduction.

In the unrealistic case where the induced power at the implant electrode is desired to be nullified, the formulation and corresponding excitation vector for the null SAR case $\mathbf{v}_{\mathrm{NS}}$ is:

$$\begin{array}{ll} \min_{\mathbf{v}} & \left\| \mathbf{B}_{\mathbf{1}}^{+}\mathbf{v} - B_{1,\mathrm{ref}}^{+}\mathbf{t} \right\|^2 \\ \text{s.t.} & \mathbf{S}_{\delta}^{T}\mathbf{E}_{\mathbf{tan}}\mathbf{v} = 0 \end{array} \Rightarrow \mathbf{v}_{\mathrm{NS}} \tag{7}$$

A final interesting case is the one where the induced power is maximized over the power dissipated in the phantom. This case would provide the maximum SAR, and its formulation and associated solution for the excitation vector $\mathbf{v}_{\mathrm{MS}}$ take the form, from [19]:

$$\max_{\mathbf{v}} \frac{\mathbf{v}^H \mathbf{E}_{\mathbf{tan}}{}^H \left(\mathbf{S}_{\delta}\mathbf{S}_{\delta}^H\right)^T \mathbf{E}_{\mathbf{tan}}\mathbf{v}}{\mathbf{v}^H \mathbf{Q}\mathbf{v}} \Rightarrow \mathbf{v}_{\mathrm{MS}} \tag{8}$$

where the 2×2 matrix $\mathbf{Q}$ is the so-called "Q-matrix" [21] to account for the dissipated power in the phantom, while superscript H stands for the conjugate transpose (Hermitian) operation.

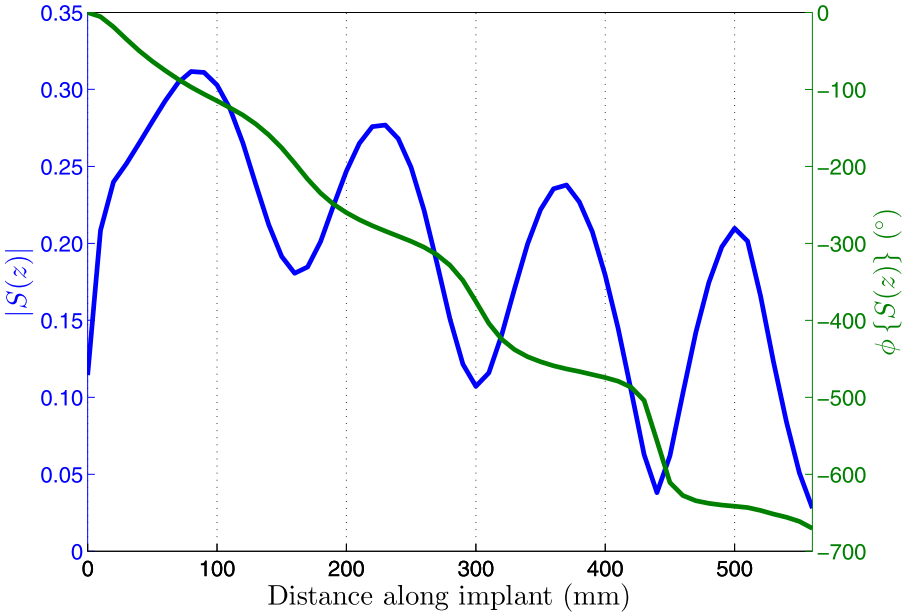

Fig. 7. Measured piece-wise transfer function at 64 MHz of the generic 550 mm implant.

Problems (6)–(8), needed to determine the desired exposure configurations, are convex optimization problems, each of them having a unique global solution that can be achieved with well-established algorithms. Specifically, problem (6) can be solved with the use of second-order cone programming and problem (7) is easily identified as a quadratic programming problem with a single equality constraint, thus having a straightforward matrix solution [13], while problem (8) can be directly cast as the maximization of a ratio of two Hermitian forms (Rayleigh quotient), whose solution is provided by an equivalent generalized eigenvalue problem [19].

2.4. Experimental validation

As shown in Fig. 4(b), the implant is mounted inside the cylindrical phantom filled with tissue simulating liquid, following a similar pathway to the one considered to extract the tangential fields from the FDTD simulation results of the computational model (see Fig. 4(a)).

Excitation vectors (solutions to the numerical optimization problems) cannot be directly used as inputs to the hardware system. However, each excitation vector produces a desired exposure configuration (fields inside the birdcage with a given input power) that is experimentally mapped by matching the value of the $\vec{B}_1$ field at a given location in the computational model with the measurement from a time-domain magnetic field probe system (TDS-B1, ZMT) [22]. To that effect, the polarization state of the magnetic field can be characterized by two parameters ϵ and τ defining the ellipticity and tilt angle of the field polarization [23]. The ellipticity (ϵ) is defined as:

$$\epsilon = \alpha \cdot \operatorname{arccot}(AR) \tag{9}$$

where AR is the axial ratio of the polarization ellipse, defined as the ratio of the magnitude of the major axis of the polarization ellipse to that of the minor axis. α indicates the rotation of the polarization ellipse, $\alpha = 1$ for left-hand rotation, α = -1 for right-hand rotation. As shown in Fig. 5, the polarization space is defined and mapped as follows: $\epsilon \in [-45^\circ, 45^\circ]$; $\tau \in [0^\circ, 180^\circ]$.

The spatial variation of the $\vec{B}_1$ field within the phantom is minimal, and is assessed in the confidence interval. Once the exposure configuration (I and Q) is matched to the target polarization, the SAR distribution around the electrode of the implant is measured with a DASY SAR probe (SPEAG) with a measurement resolution of 1 mm. The "touchless" co-registration technique [24] is used to assess the implant hotspot response with the aid of a numerically derived local power deposition distribution. The complete experimental setup with the implant inside the birdcage coil resonator and the two different probe types is shown in Fig. 6 from two different perspectives.

2.5. Confidence interval estimation

The confidence interval of the validation measurement of a given implant, exposure system, and polarization was assessed for tests performed by the IT'IS Foundation following the methodology of the GUM [25]. The validation uncertainty comprises the experimental characterization of the normalized transfer function of the generic implant (Table 1),

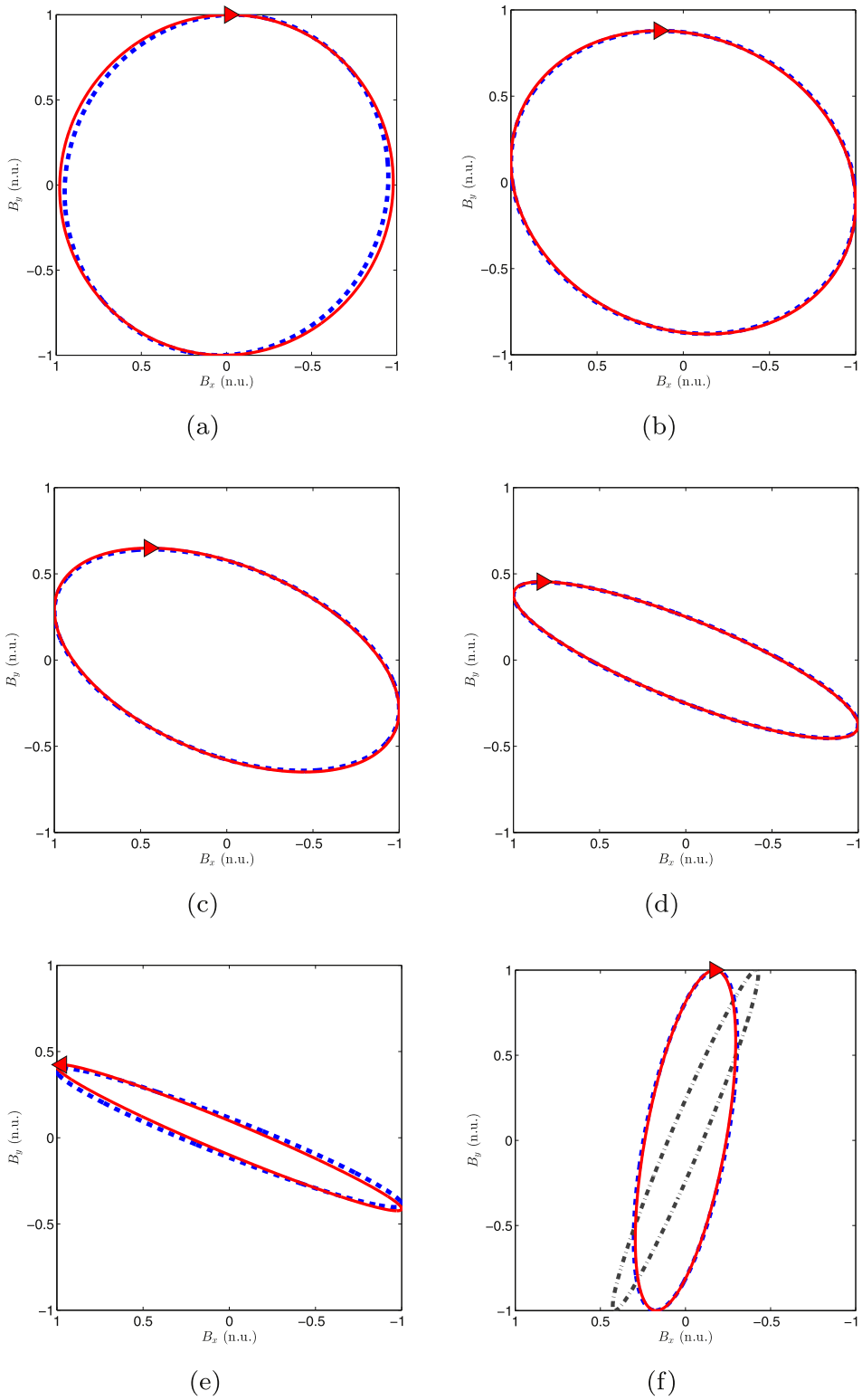

Fig. 8. Polarization ellipses in normalized units (n.u.) for the selected exposure configurations through matching the $\vec{B}_1$ field. Dashed blue line: numerically optimized. Solid red line: experimentally achieved. (a) Best homogeneity. (b) C=80%. (c) C=50%. (d) C=20%. (e) Null SAR. (f) Approximate maximum SAR, together with the maximum SAR polarization ellipse (shown in the dashed-dotted gray line), which could not be achieved by the available hardware.

Table 1
Uncertainty of the normalized transfer function model of the test item.

Source of Uncertainty	Std. Uncertainty (dB)
Analyzer drift	0.01
Cable movement	0.08
TDS linearity	0.25
Excitor positioning (x,y)	0.05
Excitor positioning (z)	0.25
Phantom boundaries	0.20
Reflected power	0.06
TSM properties	0.13
Device definition	0.05
Post-processing	0.07
Combined Std. Uncertainty ($k = 1$)	**0.45 dB**

Table 2
Combined uncertainty of incident field exposure, due to the RF coil and phantom.

Source of Uncertainty	Std. Uncertainty (dB)
$B_{1,RMS}$ drift	0.12
Phantom position	0.41
Phantom fill-height	0.12
Test item position	0.58
TSM conductivity	0.17
TSM permittivity	0.15
Polarization	0.16
TFD incident field	0.68
Combined Std. Uncertainty ($k = 1$)	**0.92 dB**

Table 3
Uncertainty of local SAR enhancement measured via radiated testing in the MITS using DASY with an EX3D SAR probe. Probe positioning as well as interpolation and averaging are nor sources of of uncertainty.

Source of Uncertainty	Std. Uncertainty (dB)
DASY SAR Enhancement	
Probe linearity	0.12
Spherical isotropy	0.35
Readout electronics	0.01
"Touchless" Co-Registration [24]	
Co-registration	0.52
Background inhomogeneity	0.29
AIMD holder	0.35
Volume integral ($\leq$-40 dB)	0.29
Grid resolution	0.14
Boundary condition ($\leq$-80 dB)	0.01
Tip modeling	0.29
Combined Std. Uncertainty ($k = 1$)	**0.89 dB**

the uncertainty of incident field to the implant from coil and phantom modeling (Table 2), and the the assessment of the SAR/deposited power under each exposure configuration (Table 3). The total validation uncertainty is given in Table 4.

3. Results

The measured piece-wise transfer function at the resonant operating frequency, incorporated as $\mathbf{S}_\delta$ in the optimization formulations of Section 2.3, is shown in Fig. 7.

The polarization ellipses of the magnetic field, measured and computed at a location placed 2 mm above the phantom center, for the six exposure configurations selected via the proposed hybrid numerical-experimental approach are shown in Fig. 8. Results show a good agreement, within the expanded validation uncertainty of Table 4, between measured and computed exposure configurations, except for the cases of null SAR (due to low signal-to-noise ratio) and when the SAR at the electrode of the implant is maximized; in the latter case, the hardware was not able to achieve the target exposure

Table 4
Estimated validation uncertainty.

Source of Uncertainty	Std. Unc. (dB)
Transfer Function Measurement (Table 1)	0.45
Coil and Phantom Modeling (Table 2)	0.92
SAR Measurement (Table 3)	0.89
Combined Std. Uncertainty ($k = 1$)	**1.36**
Expanded Uncertainty ($k = 2$)	**2.71**

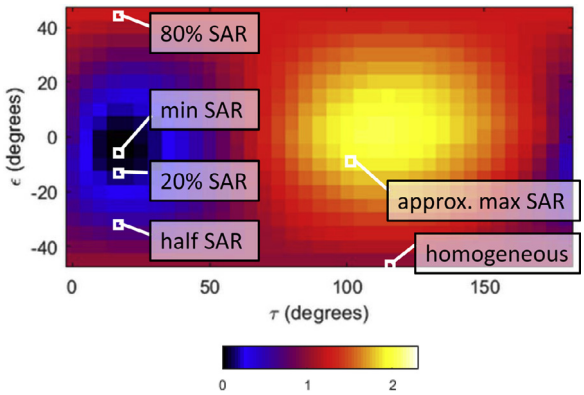

Fig. 9. Heat map of the predicted SAR reduction/increase (w.r.t. to the best homogeneity case) from the measured transfer function over the $\epsilon - \tau$ polarization space. Rectangles indicate the $\epsilon - \tau$ values for each exposure configuration, calculated from the experimentally measured polarizations in Fig. 8.

Table 5
Measured and expected reduction/increase in SAR over a 6×4 mm^2 centered at the implant electrode with the best homogeneity exposure configuration being the reference case.

ase	Change from Best Homogeneity, in dB	
	Experimental	Theoretical
Best Homogeneity	0	0
C=80%	0.45	0.97
C=50%	2.32	3.01
C=20%	6.58	6.99
Null SAR	9.41	∞
Approx. Maximum SAR	1.29	–

configuration, so the closest polarization achievable by the hardware was used (Fig. 8(f)). As expected, Fig. 8(a) shows that the best-homogeneity case is achieved for a nearly pure right-hand circular polarization.

We take the best homogeneity case as the reference point, from which we check the *in excess* (subtracting background SAR for the same exposure configuration with no implant and normalizing over whole phantom SAR) SAR reduction/increase. As first approach to validation, the $\epsilon - \tau$ values of the measurements performed over the polarization space, corresponding to the chosen SAR reductions, are shown in Fig. 9, superimposed over the numerically predicted (with the measured transfer function) ratio at the implant electrode (heatmap).

The final experimental measurement of the SAR reduction/increase in a 6×4 mm^2 zone around the electrode is carried out for validation purposes. Table 5 shows the achieved reduction for the cases C=80%, C=50%, C=20% and null SAR, as well as the increase in the aforementioned case of approximate maximum SAR. Values shown for each exposure configuration include results for the theoretical objective reduction (according to the formulations presented in Section 2.3) and the experimentally measured reduction. It can be stated that the experimentally measured reduction is coherent with the trend predicted by the objective and simulated data. Specifically, the discrepancy in the estimated reduction becomes larger, as this reduction is expected to reach very low SAR values. This is exemplified in the null SAR case, for which the experimental configuration is able to measure a reduction of nearly 10 dB.

The measured SAR distributions, ordered from the highest one (approximate maximum SAR case) to the lowest one (null SAR case) are shown in Fig. 10. The white rectangle indicates the considered area used to yield the results of Table 5. As can be seen, through proper exposure configuration selection with the proposed methodology, the actual RF-induced SAR near the implant electrode is significantly reduced.

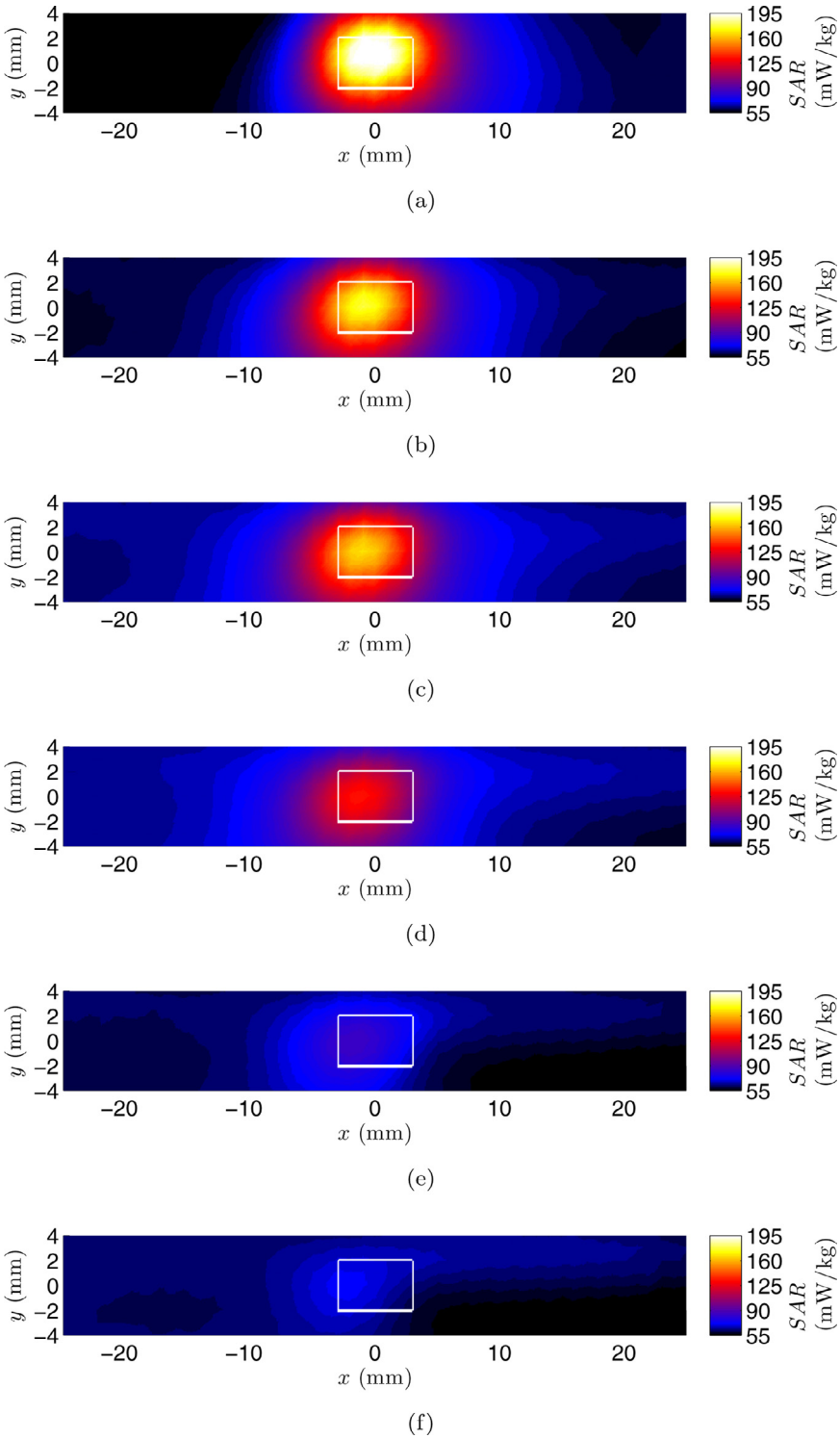

Fig. 10. Actual measured SAR distribution over a bidimensional grid of 1 mm^2 [24] for the considered cases: (a) Approximate maximum SAR. (b) Best homogeneity. (c) C=80%. (d) C=50%. (e) C=20%. (f) Null SAR. The white rectangle indicates the considered area used to yield the results of Table 5.

4. Conclusion and future work

This paper presents and experimentally validates a hybrid numerical-experimental methodology. It aims for providing a practical quasi real-time optimisation to reduce the SAR around the electrode of an elongated implant when it is exposed to RF fields during MR examinations, while minimizing the impact on the homogeneity of the circularly polarized magnetic field. The approach combines the measured transfer function of the implant, inserted into an implant-free computational model of the MR-mimicking experimental setup, together with a numerical optimization to yield the desired exposure configurations. Overall, six different scenarios were considered: the best homogeneity scenario and scenarios where the SAR at the electrode is reduced by 80%, 50% and 20%, together with two extreme scenarios where the SAR is either nullified or maximized; while minimizing the impact on $|B_1^+|$ homogeneity.

For validation purposes, an experimental setup is arranged with a usual two-channel (I and Q) birdcage coil conceived for 1.5 T MR systems operating close to 64 MHz, inside which a generic elongated implant is placed together with one time-domain magnetic field probe and one SAR probe. Measured results of the SAR distribution around the electrode of the implant are within 0.7 dB for the scenarios considered with respect to theoretical objective and numerically predicted values, well within the estimated $k = 1$ confidence interval of 1.4 dB.

The experimental validation of the optimization algorithm paves the way for its future incorporation into MR technology, e.g. performing quasi real-time optimization for multi-transmit scanners. While the transfer function approach, which is used as the basis for this optimization, is accepted as standard by practitioners and regulators worldwide it remains challenging to accurately register the actual lead path from a few pre-scan images to the pre-computed field libraries. The next step is the development and validation of such a procedure.

Acknowledgements

This work was supported by AEI/FEDER, UE (project number TEC2016-76070-C3-1-R) and the EMPIR grant 17IND01 MIMAS, which is co-funded by the European Union's Horizon 2020 research and innovation program and the EMPIR participating states. The authors would like to thank Dr. Tolga Goren from the IT'IS Foundation for his work in carrying out the confidence interval estimation, the generation of results and the critical revision and re-drafting of the manuscript. The authors would like to thank Dr. Arya Fallahi from the IT'IS Foundation and Dr. Sabine Regel from SR Scientific GmbH for their insightful comments and careful reading of the manuscript, and Dr. Maurice Cox from NPL for his review of the confidence interval estimation.

References

[1] C.D. Smith, A.V. Kildishev, J.A. Nyenhuis, K.S. Foster, J.D. Bourland, Interactions of magnetic resonance imaging radio frequency magnetic fields with elongated medical implants, J. Appl. Phys. 87 (9) (2000) 6188–6190.
[2] K.B. Baker, J.A. Tkach, J.A. Nyenhuis, M. Phillips, F.G. Shellock, J. Gonzalez-Martinez, A.R. Rezai, Evaluation of specific absorption rate as a dosimeter of MRI-related implant heating, J. Magn. Reson. Imaging 20 (2) (2004) 315–320.
[3] ISO, Assessment of the safety of magnetic resonance imaging for patients with an active implantable medical device, 2018.
[4] S.-M. Park, R. Kamondetdacha, J.A. Nyenhuis, Calculation of MRI-induced heating of an implanted medical lead wire with an electric field transfer function, J. Magn. Reson. Imaging 26 (5) (2007) 1278–1285.
[5] S. Feng, Q. Wang, C. Wen, J. Zheng, W. Kainz, J. Chen, Simplified transfer function assessment of implantable leads for MRI safety evaluations, IEEE Trans. Electromag. Compatibil. 61 (5) (2019) 1432–1437.
[6] A. Yao, E. Zastrow, E. Neufeld, M. Cabanes-Sempere, T. Samaras, N. Kuster, Novel test field diversity method for demonstrating magnetic resonance imaging safety of active implantable medical devices, Phys. Med. Biol. 65 (7) (2020) 075004.
[7] M.E. Ladd, H.H. Quick, Reduction of resonant RF heating in intravascular catheters using coaxial chokes, Magn. Reson. Med. 43 (4) (2000) 615–619.
[8] R.W. Gray, W.T. Bibens, F.G. Shellock, Simple design changes to wires to substantially reduce MRI-induced heating at 1.5 t: implications for implanted leads, Magn. Reson. Imaging 23 (8) (2005) 887–891.
[9] P. Nordbeck, I. Weiss, P. Ehses, O. Ritter, M. Warmuth, F. Fidler, V. Herold, P.M. Jakob, M.E. Ladd, H.H. Quick, W.R. Bauer, Measuring RF-induced currents inside implants: Impact of device configuration on MRI safety of cardiac pacemaker leads, Magn. Reson. Med. 61 (3) (2009) 570–578.
[10] R. Yang, J. Zheng, Y. Wang, R. Guo, W. Kainz, J. Chen, Impact of electrode structure on RF-induced heating for an AIMD implanted lead in a 1.5-Tesla MRI system, IEEE J. Electromagn. RF Microw. Med. Biol. 3 (4) (2019) 247–253.
[11] C.J. Yeung, R.C. Susil, E. Atalar, RF heating due to conductive wires during MRI depends on the phase distribution of the transmit field, Magn. Reson. Med. 48 (6) (2002) 1096–1098.
[12] Y. Eryaman, B. Akin, E. Atalar, Reduction of implant RF heating through modification of transmit coil electric field, Magn. Reson. Med. 65 (2011) 1305–1313.
[13] J. Córcoles, E. Zastrow, N. Kuster, Convex optimization of MRI exposure for mitigation of RF-heating from active medical implants, Phys. Med. Biol. 60 (18) (2015) 7293.
[14] J. Zheng, Z. Wang, Q. Wang, S. Hu, Z. Gu, W. Kainz, J. Chen, Developing AIMD models using orthogonal pathways for MRI safety assessment, IEEE Trans. Electromag. Compatibil. 62 (6) (2020) 2689–2695.
[15] Z. Wang, S.H. Oh, M.B. Smith, C.M. Collins, RF shimming considering both excitation homogeneity and SAR, in: Proc. Intl. Soc. Mag. Reson. Med., 2007, p. 1022.
[16] C.A.T. Van den Berg, B. van den Bergen, J.B. Van de Kamer, B.W. Raaymakers, H. Kroeze, L.W. Bartels, J.J.W. Lagendijk, Simultaneous B1+ homogenization and specific absorption rate hotspot suppression using a magnetic resonance phased array transmit coil, Magn. Reson. Med. 57 (3) (2007) 577–586.
[17] L. Tang, Y.-K. Hue, T.S. Ibrahim, Studies of RF shimming techniques with minimization of RF power deposition and their associated temperature changes, Concepts Magn. Reson. B 39 (1) (2011) 11–25.
[18] M. Murbach, E. Neufeld, E. Cabot, E. Zastrow, J. Córcoles, W. Kainz, N. Kuster, Virtual population-based assessment of the impact of 3 tesla radiofrequency shimming and thermoregulation on safety and b1+ uniformity, Magn. Reson. Med. 76 (3) (2016) 986–997.
[19] J. Córcoles, E. Zastrow, N. Kuster, On the estimation of the worst-case implant-induced RF-heating in multi-channel MRI, Phys. Med. Biol. 62 (12) (2017) 4711.

[20] K. Setsompop, L. Wald, V. Alagappan, B. Gagoski, E. Adalsteinsson, Magnitude least squares optimization for parallel radio frequency excitation design demonstrated at 7 Tesla with eight channels, Magn. Reson. Med. 59 (4) (2008) 908–915.
[21] I. Graesslin, H. Homann, S. Biederer, P. Boernert, K. Nehrke, P. Vernickel, G. Mens, P. Harvey, U. Katscher, A specific absorption rate prediction concept for parallel transmission MR, Magn. Reson. Med. 68 (5) (2012) 1664–1674.
[22] S. Kuhn, B. Kochali, N. Kuster, Active electro-optical probe system for B1-field polarization mapping in magnetic resonance imaging systems, EMC'14/Tokyo (2014).
[23] J.D. Kraus, K.R. Carver, Electromagnetics, a.o: McGraw-Hill, New York, 1973.
[24] A. Yao, E. Zastrow, N. Kuster, Data-driven experimental evaluation method for the safety assessment of implants with respect to RF-induced heating during MRI, Radio Sci. 53 (6) (2018) 700–709.
[25] Joint Committee for Guides in Metrology (JCGM), JCGM 100:2008: Evaluation of Measurement Data – Guide to the Expression of Uncertainty in Measurement, JCGM, 2008.